

# Alternative curved-boundary treatment for the lattice Boltzmann method and its application in simulation of flow and potential fields

O. R. Mohammadipoor\* and H. Niazmand†

*Ferdowsi University of Mashhad, Mechanical Engineering Department, Mashhad, Iran*

S. A. Mirbozorgi‡

*University of Birjand, Mechanical Engineering Department, Birjand, Iran*

(Received 30 June 2013; revised manuscript received 25 September 2013; published 24 January 2014)

Since the lattice Boltzmann method originally carries out the simulations on the regular Cartesian lattices, curved boundaries are often approximated as a series of stair steps. The most commonly employed technique for resolving curved-boundary problems is extrapolating or interpolating macroscopic properties of boundary nodes. Previous investigations have indicated that using more than one equation for extrapolation or interpolation in boundary conditions potentially causes abrupt changes in particle distributions. Therefore, a curved-boundary treatment is introduced to improve computational accuracy of the conventional stair-shaped approximation used in lattice Boltzmann simulations by using a unified equation for extrapolation of macroscopic variables. This boundary condition is not limited to fluid flow and can be extended to potential fields. The proposed treatment is tested against several well-established problems and the solutions order of accuracy is evaluated. Numerical results show that the present treatment is of second-order accuracy and has reliable stability characteristics.

DOI: [10.1103/PhysRevE.89.013309](https://doi.org/10.1103/PhysRevE.89.013309)

PACS number(s): 47.11.-j, 05.20.Dd, 47.10.-g

## I. INTRODUCTION

In recent years, the lattice Boltzmann method (LBM) has attracted considerable attention as an alternative numerical method for simulating various physical problems. In contrast to the conventional computational fluid dynamics (CFD) methods where macroscopic variables, such as velocity, pressure, and density, are obtained by solving the Navier-Stokes (NS) equations, the LBM solves the kinetic equation for particle distribution functions. The macroscopic variables can then be obtained by evaluating the hydrodynamic moments of the distribution functions. In comparison with conventional numerical approaches, the LBM changes the target equation from a nonlinear system to a semilinear one, which provides many distinct advantages such as simple formulation, favorable parallel computing structure, and capability in dealing with complex geometries. This idea allows the LBM to have great potential not only as a NS solver but also as a powerful numerical technique in a large variety of scientific researches and engineering applications [1–5]. However, the LBM suffers from more unknown variables at boundaries than the conventional CFD methods. Moreover, the LBM fails to directly simulate curved boundaries, since a rectangular lattice is used for simulations.

One of the most often used boundary conditions is the bounce-back rule [6,7], which makes the LBM suitable for simulating fluid flows in complicated geometries. Nevertheless, the bounce-back scheme is only first-order accurate [7]. To improve its accuracy, different schemes have been proposed, such as the halfway bounce-back scheme [7]; the nonequilibrium bounce-back scheme [8]; local thermohydrodynamic equilibrium assumption for the missing distribution

functions [9]; the extrapolation scheme [10]; the utilization of the immersed boundary treatments [11–13]; and the reconstruction of the distribution functions from the density, velocity, and rate of strain [14]. In dealing with complex geometries, curved boundaries are represented by a series of stair steps, which are more involved to improve the accuracy of the stair-shaped approximation. Filippova and Hänel [15] were the first to present a curved-boundary treatment for the LBM. Their model enabled curved walls to be treated with second-order accuracy but was somewhat unstable. To improve the numerical stability, Mei *et al.* [16,17] presented an improved curved-boundary condition based on the Filippova and Hänel scheme. Bouzidi *et al.* [18] proposed a method for treating curved boundaries by combining the bounce-back rule with an interpolation approach. Lallemand and Luo [19] applied the same approach to treat moving boundary problems. Guo *et al.* [20] extended the method developed by Chen *et al.* [10] to propose an alternative treatment for curved walls in LBM.

In dealing with curved boundaries in the regular Cartesian grid, the boundary is not necessarily aligned with grid lines. In most of the previous studies [15–20], two equations are required to treat the boundary condition according to the distance of the curved boundary from the boundary nodes, which has significant impact on the numerical stability and accuracy of simulations [21]. It may also cause abrupt changes in distribution functions during the switching between equations [22,23]. Recently, Kao and Young [22] proposed a unified interpolation-free treatment for modeling curved boundaries using an appropriate local refinement grid technique with bounce-back scheme at boundary nodes. Yu *et al.* [23] also proposed a unified treatment for curved boundaries following the concept introduced by Bouzidi *et al.* [18]. Verschaeve and Müller [24] extended the no-slip boundary condition developed by Latt *et al.* [14] to curved geometries.

Although all mentioned studies [15–20,22–24] provide a second-order accurate treatment of curved boundaries, they

\*o.r.mohammadipoor@gmail.com

†niazmand@um.ac.ir

‡samirbozorgi@birjand.ac.ir

suffer from some drawbacks such as unstable regions [15–17] or instability due to switching between interpolation or extrapolation equations [15–20]. Most of these boundary treatments [15–19,22,23] are based on the bounce-back scheme, which limits applicability of these boundary treatments to fluid flow and adiabatic thermal boundaries. Furthermore, since all distribution functions are not involved in the bounce-back rules, undesirable slip velocity may happen on boundary nodes [23]. In this paper, a new boundary condition scheme is developed for handling curved boundaries, while providing second-order accuracy. This new boundary condition treats curved boundaries in two steps: extrapolation and implementation. In the first step, the macroscopic property is extrapolated at boundary nodes using a unified equation to satisfy the required condition at curved walls. The extrapolation process is a geometrical calculation and can be applied to any macroscopic properties such as velocity, pressure, or temperature. The next step is the implementation, which describes how we should define distribution functions at boundary nodes to satisfy the extrapolated macroscopic property at boundary nodes. Here we specifically focused on velocity fields and extended the boundary condition of Zou and He [8] to arbitrary two-dimensional (2D) geometries. It must be emphasized that this extension directly provides a no-slip boundary condition for simple geometries such as straight walls and corners; however, in combination with the above-mentioned extrapolation scheme it models curved boundaries. The rest of the paper is organized as follows: in Sec. II, the lattice Boltzmann model for flow field is presented. In Sec. III, a new boundary treatment strategy is discussed for curved boundaries. In Sec. IV, a new no-slip boundary condition is proposed based on the Zou and He scheme for the LBM. In Sec. V, benchmark tests are discussed and, finally, some conclusions are provided in Sec. VI.

## II. THE LATTICE BOLTZMANN METHOD

Although the lattice Boltzmann equation is historically originated from the lattice gas automata method [25], it can be viewed as a special finite difference form of the continuous Boltzmann kinetic equation [26]. The main objective of the lattice Boltzmann equation is the particle distribution function  $f$ , which corresponds to the probability of finding a particle at a given location  $\mathbf{r}$  with a given velocity  $\xi$ . According to the lattice Boltzmann equation, the evolution of the distribution function  $f$  is given by

$$\frac{\partial f(\mathbf{r}, \xi, t)}{\partial t} + \xi \cdot \nabla f(\mathbf{r}, \xi, t) = \Omega, \quad (1)$$

where  $\Omega$  is the collision operator. In the discrete velocity space and without affecting the conserved hydrodynamic moments, the microscopic velocity  $\xi$  is discretized into  $q$  lattice vectors  $\{\mathbf{c}_0, \mathbf{c}_1, \dots, \mathbf{c}_{q-1}\}$ . Consequently, distribution function  $f$  and the collision operator  $\Omega$  are also discretized as follows:

$$\frac{\partial f_i(\mathbf{r}, t)}{\partial t} + \mathbf{c}_i \cdot \nabla f_i(\mathbf{r}, t) = \Omega_i \quad (i = 0, 1, \dots, q-1). \quad (2)$$

In this paper, a nine-velocity 2D lattice, denoted as the D2Q9 model, has been used. In this model, the discrete velocity

set is given as [27]

$$\mathbf{c}_i = w(0,0) \quad (i = 0), \quad (3a)$$

$$\mathbf{c}_i = (\cos \theta_i, \sin \theta_i)c \left( \theta_i = \frac{(i-1)\pi}{2}, i = 1-4 \right), \quad (3b)$$

$$\mathbf{c}_i = \sqrt{2}(\cos \theta_i, \sin \theta_i)c \left( \theta_i = \frac{(i-1)\pi}{2} + \frac{\pi}{4}, i = 1-4 \right). \quad (3c)$$

In the above equation,  $c = \delta_x/\delta_t$  is the particle streaming speed,  $\delta_x$  is the lattice space, and  $\delta_t$  is the time step size. To solve the distribution function numerically, Eq. (2) is discretized with time step and lattice space into

$$f_i(\mathbf{r} + \mathbf{c}_i \delta_t, t + \delta_t) - f_i(\mathbf{r}, t) = \Omega_i. \quad (4)$$

The most popular model, the lattice Bhatnagar-Gross-Krook (LBGK) [28] is used in this paper, which approximates the collision operator as a relaxation of the distribution function  $f$  towards a local equilibrium distribution  $f^{\text{eq}}$ ,

$$\Omega_i = \frac{1}{\tau} (f_i^{\text{eq}}(\mathbf{r}, t) - f_i(\mathbf{r}, t)). \quad (5)$$

In the above equation,  $\tau$  is a dimensionless relaxation time and related to the kinetic viscosity of the fluid. The equilibrium distribution,  $f^{\text{eq}}$ , is a low Mach number expansion of the Maxwell-Boltzmann distribution and is written as [26]

$$f_i^{\text{eq}} = w_i \rho \left[ 1 + \frac{\mathbf{c}_i \cdot \mathbf{U}}{C_s^2} + \frac{(\mathbf{c}_i \cdot \mathbf{U})^2}{2C_s^4} - \frac{U^2}{2C_s^2} \right], \quad (6a)$$

$$\begin{aligned} w_i &= 4/9 \quad (i = 0) \\ w_i &= 1/9 \quad (i = 1-4) \\ w_i &= 1/36 \quad (i = 5-8), \end{aligned} \quad (6b)$$

where  $\mathbf{U}$  is the macroscopic velocity vector,  $\rho$  is mass density, and  $C_s = c/\sqrt{3}$  is the speed of sound. The macroscopic quantities in the LBM such as mass density and velocity are defined as moments of the distribution function,

$$\rho = \sum_i f_i, \quad (7)$$

$$\mathbf{U} = \frac{1}{\rho} \sum_i f_i \mathbf{c}_i. \quad (8)$$

In simulation of incompressible flows in a low Mach-number regime, the pressure  $p$  can be calculated by the equation of state of an ideal gas,

$$p = \rho C_s^2. \quad (9)$$

Through the Chapman-Enskog multiscale analysis, the kinematic viscosity  $\nu$  is related to the dimensionless relaxation time as follows [25]:

$$\nu = \left( \tau - \frac{1}{2} \right) C_s^2 \delta t. \quad (10)$$

## III. IMPLEMENTATION OF CURVED BOUNDARIES

The LBM scheme, including collision and propagation steps, is originally defined for equidistant Cartesian grids. For a curved geometry, this scheme requires approximation

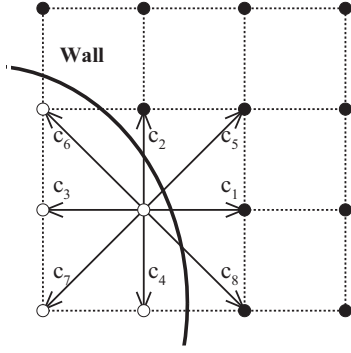


FIG. 1. The D2Q9-lattice intersected by a curved wall boundary.

of the curved solid boundaries by the nodes nearest the curved boundaries. Therefore, integrity of geometry cannot be preserved because a series of stair steps must be simulated instead of a curved boundary.

In this section, a new scheme is developed to implement curved boundaries in the regular Cartesian grid. When a complex geometry is modeled by the LBM, the physical curved boundaries may not coincide with the lattice points, as shown in Fig. 1. In this situation, nodes of the lattice can be divided into two groups: nodes located inside the fluid domain denoted as “fluid nodes” and nodes located outside the fluid domain called as “solid nodes.” In order to avoid any confusion, we will use the word “wall” in referring to the physical boundary and “lattice link” to designate directions of lattice velocities. We will also define “boundary nodes” as nodes located in the solid domain with a lattice link intersected by the wall. Obviously, from solid nodes, only boundary nodes affect the fluid domain and must be involved in the boundary condition scheme. Hereafter, we will use the subscript “b” to refer to quantities associated with boundary nodes.

The strategy of the present curved-boundary treatment is to properly extrapolate macroscopic properties at boundary nodes to obtain accurate values on the wall. Obviously, at least two reference points are needed to do the extrapolation, which are commonly taken in the fluid domain (fluid reference) and on the wall adjust to boundary node (wall reference).

It is worth mentioning that in all previous studies [15–20,22–24] both reference points have been selected along lattice links. Since the normal direction is not necessarily along with a lattice velocity direction, applying a von Neumann boundary condition in previous studies requires extra calculations to maintain second-order accuracy.

In this work, reference points are not limited to lattice links and points as shown in Fig. 2. The intersection point of the wall-normal vector passing through the boundary node is considered as the wall reference denoted by  $P_{\text{wall}}$ . The fluid reference,  $P_f$ , is chosen along the wall-normal direction with a distance of  $2\delta_x - \Delta$  from  $P_{\text{wall}}$ , where  $\Delta$  is “boundary distance” defined as the distance of the wall reference from the boundary node. The third reference point  $P_{ff}$  can be defined in a similar way, with distance of  $4\delta_x$  from the boundary node as depicted in Fig. 2

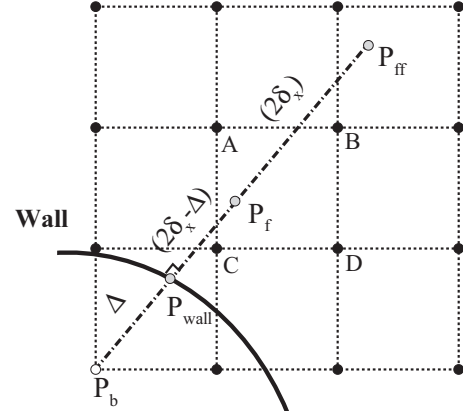


FIG. 2. Layout of reference points corresponding to the boundary point  $P_b$ : wall reference  $P_{\text{wall}}$  on the wall and along with the wall-normal vector; first fluid reference  $P_f$  with distance of  $2\delta_x - \Delta$  from  $P_{\text{wall}}$ ; second fluid reference  $P_{ff}$  with distance of  $2\delta_x$  from  $P_f$ .

Calculation of fluid property  $M_b$  at the boundary node is straightforward as follows:

$$M_b^{(1)} = \frac{2}{2 - \Delta^*} M_{\text{wall}} - \frac{\Delta^*}{2 - \Delta^*} M_f, \quad (11)$$

$$M_b^{(2)} = \frac{8}{(2 - \Delta^*)(4 - \Delta^*)} M_{\text{wall}} - \frac{2\Delta^*}{(2 - \Delta^*)} M_f + \frac{\Delta^*}{(4 - \Delta^*)} M_{ff}. \quad (12)$$

In above equations,  $M_b^{(1)}$  and  $M_b^{(2)}$  are extrapolated macroscopic values obtained from linear [Eq. (11)] and quadratic [Eq. (12)] schemes, respectively, and  $\Delta^* = \Delta/\delta_x$  is a dimensionless boundary distance. For a Dirichlet boundary condition, the fluid property of  $M_{\text{wall}}$  at the point  $P_{\text{wall}}$  is given and an estimate of macroscopic property at the fluid reference, e.g.,  $M_f$  can also be found by evaluating the bilinear interpolation between four surrounding fluid nodes of A, B, C, and D as shown in Fig. 2.

$$M_f = \frac{M_C}{\delta_x^2} (x_B - x_f)(y_B - y_f) + \frac{M_D}{\delta_x^2} (x_f - x_A)(y_A - y_f) + \frac{M_A}{\delta_x^2} (x_D - x_f)(y_f - y_D) + \frac{M_B}{\delta_x^2} (x_f - x_C)(y_f - y_C). \quad (13)$$

It must be noted that when the  $x$  or  $y$  value of a reference point is equal to that of a surrounding fluid node, the above equation decreases to the interpolation between two surrounding fluid nodes. In some previous studies [15–20], since the reference points are enforced to be on a lattice link, two equations along with a switching scheme were required to treat the boundary condition. This switching may lead to an abrupt variation in distribution functions [22,23] or may affect the accuracy of simulations [21]. However, the present scheme requires a single equation [Eqs. (11) or (12)] to extrapolate boundary quantities independent of the wall position. From Eqs. (11) and (12), the quadratic extrapolation provides more

accurate results but our numerical experiments showed that using Eq. (12) may lead to instabilities for  $\Delta^* > 1$  when the dimensionless relaxation time is close to  $\tau = 0.6$ . As a remedy, we offer the following combination of linear and quadratic extrapolations to balance between accuracy and stability:

$$M_b = \frac{2 - \Delta^{*2}}{2} M_b^{(2)} + \frac{\Delta^{*2}}{2} M_b^{(1)}. \quad (14)$$

In cases with poor grid resolutions, care must be taken about choosing lattice space to have  $\delta_x$  reasonably smaller than minimum wall curvature radius. The extrapolation process as discussed above is a geometrical calculation and can be used for any macroscopic property such as velocity, pressure, or temperature. However, simulation of curved boundaries requires the implementation of the extrapolated macroscopic value ( $M_b$ ) at boundary nodes using the lattice Boltzmann equations. In the next section, this has been done for boundary velocity  $\mathbf{U}_b$  as an example.

#### IV. NO-SLIP BOUNDARY CONDITION

In flow field simulations, one of the most important properties at boundary nodes is velocity. Simulation of curved boundaries in flow field requires a boundary treatment to apply the desirable velocity ( $\mathbf{U}_b = u_x \hat{\mathbf{i}} + u_y \hat{\mathbf{j}}$ ) on boundary nodes. Here, we extend the Zou and He [8] scheme to provide a no-slip boundary condition for arbitrary 2D geometries. Specification of velocity boundary condition is performed through distribution functions illustrated in Fig. 3 for a typical boundary node on a wall in the D2Q9 lattice. Three distribution functions entering the fluid domain from the solid region, shown by dashed vectors, are unknown. Boundary condition treatments in LBM are mainly focused on the calculation of these typical unknown distribution functions.

The distribution function on each boundary node can be decomposed into the equilibrium ( $f^{\text{eq}}$ ) and nonequilibrium ( $f^{\text{neq}}$ ) parts. At a boundary node, the equilibrium parts of the unknown distribution functions can be obtained from macroscopic values of  $\rho$  and  $\mathbf{U}$  by Eq. (6). Zou and He [8] assumed that the bounce-back condition holds only for the nonequilibrium parts of distribution functions in the direction normal to the boundary. To determine the nonequilibrium parts of unknown distribution functions, we extend this idea to all unknown directions by taking the nonequilibrium parts from the opposite known directions. Consequently, an approximation of unknown distribution functions can be constructed by adding equilibrium and nonequilibrium parts. For example, this approximation for  $f_2$ ,  $f_5$ , and  $f_6$  at the lower wall, shown

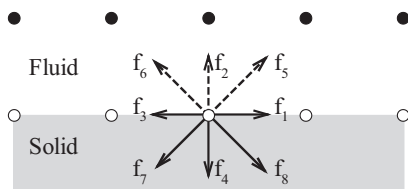


FIG. 3. Layout of distribution functions for a typical boundary node on a wall in the D2Q9 lattice.

in Fig. 3, leads to the following:

$$\begin{aligned} f_2 &= f_2^{\text{eq}} + f_4^{\text{neq}} \\ f_5 &= f_5^{\text{eq}} + f_7^{\text{neq}} \\ f_6 &= f_6^{\text{eq}} + f_8^{\text{neq}}. \end{aligned} \quad (15)$$

Since  $f_1$  and  $f_3$  are not included in the above equations, undesirable slip velocity may occur in tangential direction. As a remedy, an additional part for distribution functions is introduced, denoted as  $h_i$ . The role of  $h_i$  is to adjust the boundary node distribution functions such that the no-slip condition in all directions is satisfied,

$$\mathbf{U}_b = \frac{1}{\rho} \sum_i (f_i^{\text{eq}} + f_i^{\text{neq}} + h_i) \mathbf{c}_i. \quad (16)$$

It must be noted that the introduced function, which will be called “corrective function” hereafter, should not change the local mass density, therefore

$$\sum_{i=1}^8 h_i = 0. \quad (17)$$

This zero mass density condition can be simply satisfied with antisymmetric definition of  $h_i$  on opposite directions as follows:

$$\begin{aligned} h_1 &= -h_3 = b \\ h_2 &= -h_4 = a \\ h_5 &= -h_7 = c \\ h_6 &= -h_8 = d. \end{aligned} \quad (18)$$

According to the above equations set, there are four unknown values to evaluate  $h_i$ . Definition of velocity provides two equations,

$$\begin{aligned} b + c - d &= 0 \\ a + c + d &= 0. \end{aligned} \quad (19)$$

When distribution functions are known in opposite directions, the equality of the nonequilibrium parts also provides some equations as

$$2h_i = (f_i - f_{\text{opp}(i)}) - (f_i^{\text{eq}} - f_{\text{opp}(i)}^{\text{eq}}), \quad (20)$$

where the subscript “opp” is used to denote the opposite direction. Finally, the system of equations can be closed by setting the remained unknown corrective functions to be zero. For a boundary node on a lower wall, the corrective functions can be obtained from the following equation set:

$$\begin{aligned} b + c - d &= 0 \\ a + c + d &= 0 \\ 2b &= f_1 - f_3 - \frac{2}{3} \rho u_x \\ a &= 0. \end{aligned} \quad (21)$$

It must be noted that we can extrapolate the remained unknown corrective functions from the nearest fluid nodes instead of setting them to zero; however, these extrapolations have negligible effect on the accuracy of the scheme. Setting them to zero has the benefit of keeping the algorithm local and is equivalent to applying the pure bounce-back rule to

nonequilibrium parts. This process is not limited to flat walls; other geometries such as corners with different number of unknowns can also be treated in a similar way. The resulting systems of equations for common geometries are presented in the Appendix. The implementation of no-slip condition is completed by adding the corrective functions to Eq. (15) as follows:

$$f_i = f_i^{\text{eq}} + f_{\text{opp}(i)}^{\text{neq}} + h_i$$

$$\rightarrow \begin{cases} f_2 = f_2^{\text{eq}} + (f_4 - f_4^{\text{eq}} - h_4) + h_2 \\ f_5 = f_5^{\text{eq}} + (f_7 - f_7^{\text{eq}} - h_7) + h_5 \\ f_6 = f_6^{\text{eq}} + (f_8 - f_8^{\text{eq}} - h_8) + h_6 \end{cases} \quad (22)$$

The solution of Eq. (21) is then substituted into Eq. (22), to give the final form as follows:

$$f_2 = f_2^{\text{eq}} + (f_4 - f_4^{\text{eq}})$$

$$f_5 = f_5^{\text{eq}} + (f_7 - f_7^{\text{eq}}) - (f_1 - f_3 - 2\rho u_x/3) \quad (23)$$

$$f_6 = f_6^{\text{eq}} + (f_8 - f_8^{\text{eq}}) + (f_1 - f_3 - 2\rho u_x/3),$$

Note that in the above process, the value of the particle density  $\rho$  has to be computed. As discussed in previous studies [8,14], the value of density can be determined on straight walls from the known distribution functions and velocity value. However, the available information on a boundary node may not be sufficient for the evaluation of the density on more complex geometries. In these situations, a common method is to extrapolate the density from the neighboring fluid node. However, this extrapolation enforces a zero pressure gradient along the extrapolation direction and also requires information from neighboring boundary nodes. Obviously, zero pressure gradient is not applicable, where the body force has a nonzero component along the extrapolation direction. Verschaeve and Müller [24] defined a new function  $g_i$ , as the equilibrium distribution with unit density  $g_i = f_i^{\text{eq}}(1, \mathbf{U})$  to produce several approximations for local mass density. Using  $g_i$ , we introduce a new equation to approximate mass density, which is purely local to boundary nodes and is independent of boundary shape, in the presence or lack of body forces. This new mass density equation is based on the equality of nonequilibrium parts in opposite directions for unknown distribution functions and can be expressed as

$$\rho = \frac{\sum_j f_j + \sum_k f_{\text{opp}(k)}}{1 + \sum_k (g_{\text{opp}(k)} - g_k)}, \quad (24)$$

where  $j$  and  $k$  indexes the known and unknown directions, respectively. It must be considered that it is always possible to use any other approximation to determine the density of boundary nodes. To conclude this section, the implementation of no-slip condition is summarized below:

Step (1): Compute the mass density using Eq. (24) or other approximations.

Step (2): Compute the equilibrium parts of the unknown distribution functions by using the mass density obtained from step (1) and desired boundary velocity  $\mathbf{U}_b$ .

Step (3): Compute the corrective functions.

Step (4): Construct the value of the unknown distribution functions by adding equilibrium, nonequilibrium, and corrective parts,  $f_i = f_i^{\text{eq}} + f_{\text{opp}(i)}^{\text{neq}} + h_i = f_{\text{opp}(i)} + (f_i^{\text{eq}} - f_{\text{opp}(i)}^{\text{eq}}) + (h_i - h_{\text{opp}(i)})$ .

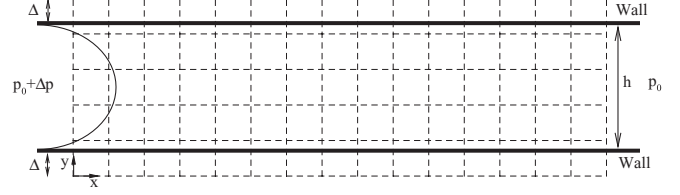


FIG. 4. Layout of the lattice in channel flow simulations with arbitrary boundary distance  $\Delta$ .

## V. VALIDATION

In this section, we present the results of benchmark tests performed to validate the curved-boundary implementation and no-slip boundary condition outlined above. We considered the following test cases: pressure-driven channel flows, flow between two rotating circular cylinders, uniform flow over a circular cylinder, and the solution of the Laplace equation in a concentric annulus.

All validation cases are carried out for 2D flows and Eq. (14) is utilized to extrapolate variables for boundary nodes. To assess the numerical error of the lattice Boltzmann solutions, the following relative error is defined:

$$E_r = \sqrt{\frac{1}{N} \sum_N (R_{\text{Analytic}} - R_{\text{Num}})^2}, \quad (25)$$

where  $R_{\text{Num}}$  and  $R_{\text{Analytic}}$  indicate the numerical and analytical results, respectively, and  $N$  is the number of nodes.

### A. Pressure-driven channel flow

A fully developed pressure-driven flow in a 2D channel is a classic case to validate no-slip boundary conditions. Furthermore, it can be used to evaluate the accuracy and stability of the developed extrapolation scheme. In this problem, the wall locations are moved from boundary nodes as shown in Fig. 4 and velocity extrapolations in addition to the no-slip boundary conditions are applied on walls.

The flow is characterized by a constant pressure drop along the channel, which is applied by using pressure boundary conditions [8] at the channel inlet and outlet. The analytical velocity distribution is given by [29]

$$\frac{u}{U_{\text{max}}} = 4\frac{y}{h} \left(1 - \frac{y}{h}\right), \quad (26)$$

where  $h$  is the channel height and the maximum value of velocity is defined as  $U_{\text{max}} = -\nabla p h^2 / 8\mu$ . In this simulation, the dimensionless relaxation time  $\tau$ , is set to 0.75 and the pressure drop is adjusted to keep the Reynolds number constant at  $\text{Re} = 5$ .

In order to assess the stability of the present extrapolation scheme, the distance of the wall from boundary nodes is taken in the range of  $0-1.25\delta_x$ . Figure 5 shows the velocity profile relative error  $E_{r(u)}$  variations as a function of lattice resolution for a number of different boundary distances. The lattice resolution  $N_R$  is defined as the number of nodes along the channel height. Linear fitting of error data indicates second-order overall accuracy.

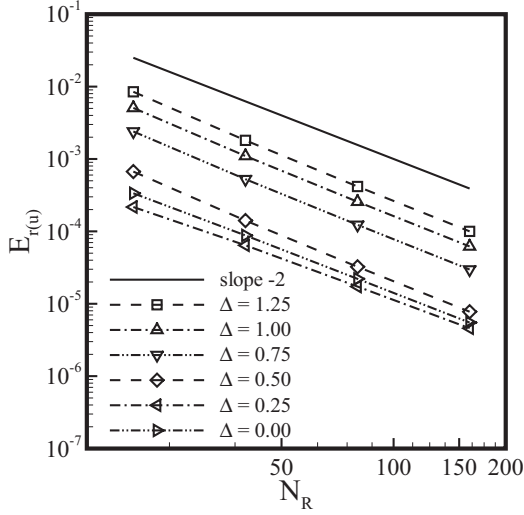


FIG. 5. Velocity relative errors as a function of lattice resolution for several boundary distances for a flat channel flow at  $Re = 5$ .

A comprehensive numerical study has been performed to assess the accuracy of the present scheme wall velocity predictions. In this regard, the predicted wall-slip velocities ( $u_{\text{wall}}$ ) for a pressure-driven channel flow have been compared with four commonly used curved-boundary schemes developed by Mei *et al.* [16], Bouzidi *et al.* [18], Yu *et al.* [23], and Guo *et al.* [20]. To guarantee an equal treatment, the same boundary distance and grid resolution ( $N_R = 40$ ) are used for all cases at  $Re = 5$ . Since the velocity profile is parabolic; a second-order extrapolation is adequate to determine wall-slip velocity for all cases.

Figure 6 presents wall-slip velocities as a function of various dimensionless relaxation time and boundary distance values for present treatment using Eq. (14). For comparison, wall velocity predictions related to the above mentioned schemes are also included.

From Fig. 6(a), it can be observed that the present treatment is distinctly more accurate than other approaches where wall coincides with boundary nodes ( $\Delta^* = 0$ ). This is also true when boundary distance increases to  $\Delta^* = 0.25$  in Fig. 6(b). Furthermore, one can see from Fig. 6(b) that the wall-slip velocity for previous schemes [16,18,20,23] reaches its minimum value when the dimensionless relaxation time is about  $\tau = 0.8$  and then increases at higher values of the dimensionless relaxation time. Clearly, there is no dependency between wall-slip velocity and dimensionless relaxation time for the present boundary treatment. This is due to the fact that, in the present boundary scheme, the boundary nodes are forced by corrective functions to have the desirable velocity ( $U_b$ ) independent of the  $\tau$  value. For other values of  $\Delta^*$ , as shown in Figs. 6(c) and 6(d), the present scheme provides a better performance over large variations of the dimensionless relaxation time as compared to other schemes.

It must be emphasized that the accuracy problem of boundary conditions is usually more visible at lower grid resolutions. Therefore, the accuracy of the present boundary treatment has been compared with previous schemes [16,18,20,23] for  $N_R = 17$ , which is the minimum allowed grid resolution in the incompressible limit ( $Ma < 0.3$ ) for the considered  $Re = 5$ . In

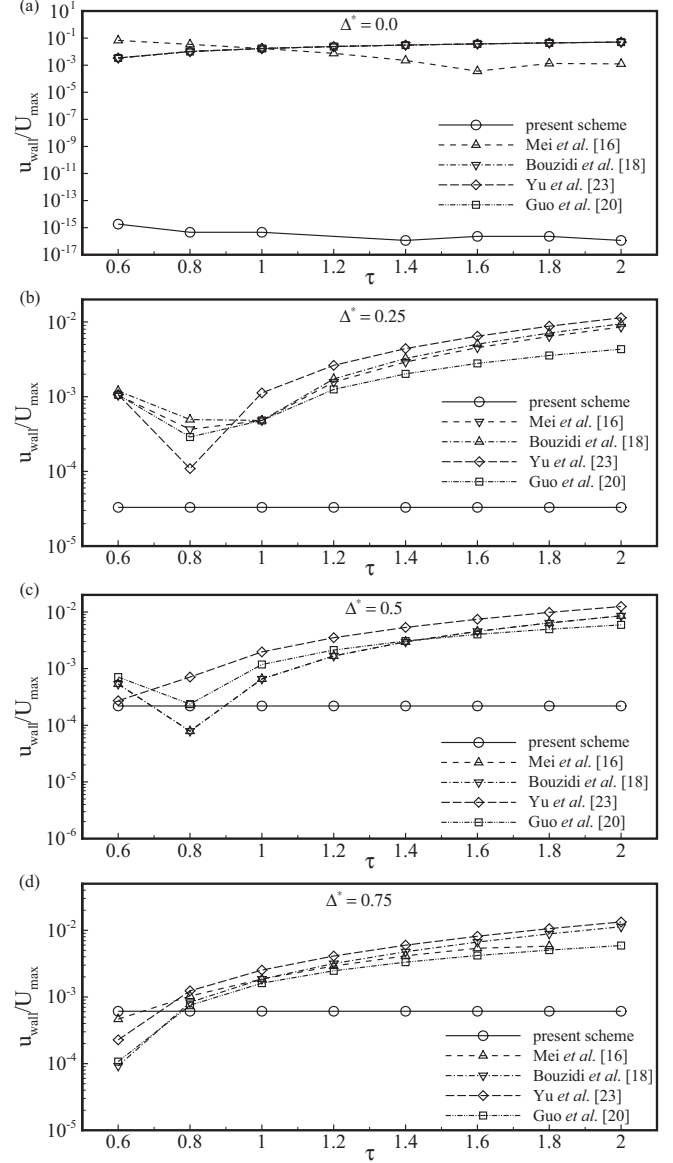


FIG. 6. Comparison of wall-slip velocities for different boundary schemes as a function of dimensionless relaxation time for a flat channel flow at  $Re = 5$  and  $N_R = 40$  for a variety of boundary distances: (a)  $\Delta^* = 0$ , (b)  $\Delta^* = 0.25$ , (c)  $\Delta^* = 0.5$ , and (d)  $\Delta^* = 0.75$ .

Fig. 7 the wall-slip velocity has been presented as a function of various dimensionless relaxation time for a single value of  $\Delta^* = 0.75$  as a sample.

Clearly, the variation trends for all schemes are quite similar to what are observed in Fig. 6(c), except for an increase of about an order of magnitude in wall slip velocities, which is expected due to the lower grid resolution. It is also worth mentioning that in the examined geometry shown in Fig. 4 all fluid reference points are exactly located on the top of grid points and, therefore, the bilinear interpolation scheme [Eq. (13)] has not been involved in the simulation process. However, for an inclined flat channel as shown in Fig. 8, fluid reference points are nonuniformly distributed among the grid points. As a test case, the inclination angle is set to be  $a/b = 1/3$  for flow conditions similar to those of the straight channel for grid resolution of 40.

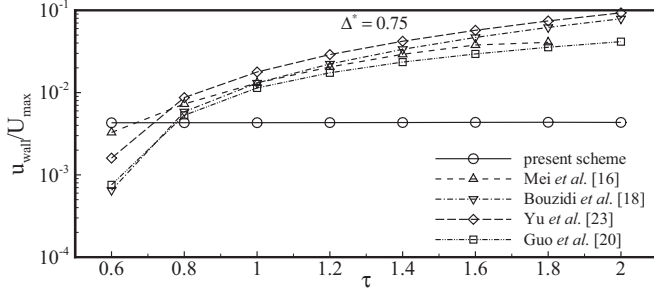


FIG. 7. Comparison of wall-slip velocities for different boundary schemes as a function of dimensionless relaxation time for a flat channel flow at  $Re = 5$  and  $N_R = 17$  for boundary distance of  $\Delta^* = 0.75$ .

Velocity vectors are presented at some typical locations along the channel in Fig. 8. It is interesting to note that the velocity profiles at the inlet and outlet are along the normal to their cross sections, where applied pressures act. However, the flow adjusts itself with channel walls and becomes fully developed shortly after the entrance effects are disappeared. Clearly, a velocity profile in a cross section normal to the channel walls in the fully developed region is required for validation. Figure 9 compares the analytical profile [Eq. (26)] with numerical velocity profiles in three cross sections of A-A, B-B, and C-C located in the quarter, half, and three-quarter channel lengths, respectively, where excellent agreements are observed for all cross sections.

Figure 10 shows the average wall-slip velocity for the inclined channel flow as a function of grid resolution, which indicates the second-order overall accuracy.

**B. Flow between two rotating circular cylinders**

To demonstrate the capability of the present boundary treatment for more complex geometries, flow between two rotating cylinders is simulated for different Reynolds number  $Re = R_i \omega (R_o - R_i) / \nu$  of 6, 8, and 10. In these simulations, the inner cylinder with radius  $R_i = 1$  cm is rotating at a constant angular velocity of  $\omega$  and the outer cylinder with radius  $R_o = 2$  cm is kept stationary. This problem is a good benchmark test to examine the accuracy and efficiency of the proposed boundary treatment in the simulation of moving and stationary curved boundaries. Furthermore, simulation of pressure field is rather complicated in this geometry due to the centripetal body force, which is completely along the wall-normal vector

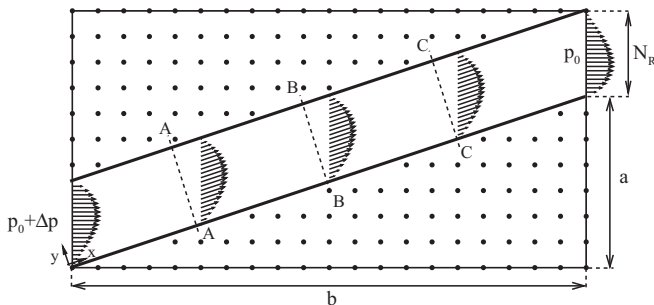


FIG. 8. Schematic of the lattice in an inclined flat channel.

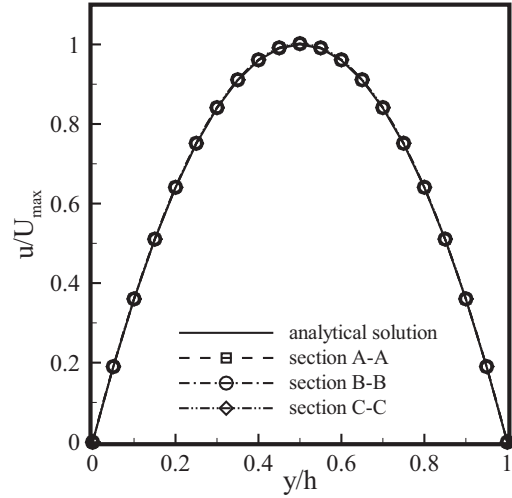


FIG. 9. Comparison between numerical and analytical velocity profiles for an inclined flat channel flow at three cross sections of A-A, B-B, and C-C.

and, therefore, extrapolation of density from neighboring fluid nodes as the most common approximation of density is not valid anymore. There is an analytical solution to the NS equations for this flow. The transversal velocity  $U_\theta$  is given by [29]

$$\frac{U_\theta(r)}{U_0} = \frac{\beta}{1 - \beta^2} \left( \frac{R_o}{r} - \frac{r}{R_o} \right), \tag{27}$$

where  $U_0 = R_i \omega$  is the reference velocity and  $\beta = R_i / R_o$ . Determining the pressure constant by imposing  $p(R_o) = 0$ , the pressure distribution can be obtained from the following equation [29]:

$$\frac{p(r)}{\rho U_0^2} = \frac{1}{2} \left( \frac{\beta}{1 - \beta^2} \right)^2 \left[ \frac{r^2}{R_o^2} - \frac{R_o^2}{r^2} - 4 \ln \frac{r}{R_o} \right]. \tag{28}$$

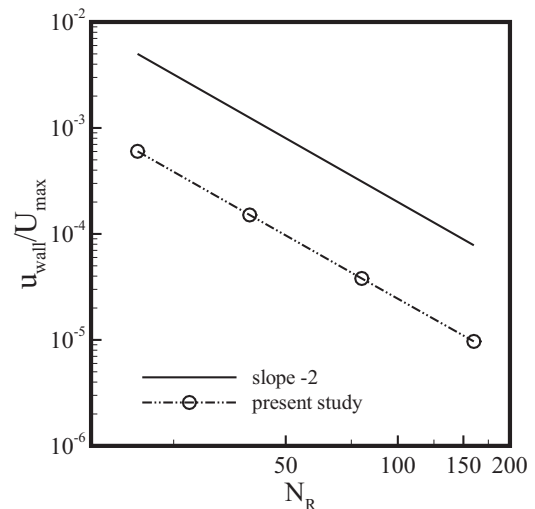


FIG. 10. Wall-slip velocity as a function of lattice resolution for an inclined flat channel flow at  $Re = 5$ .

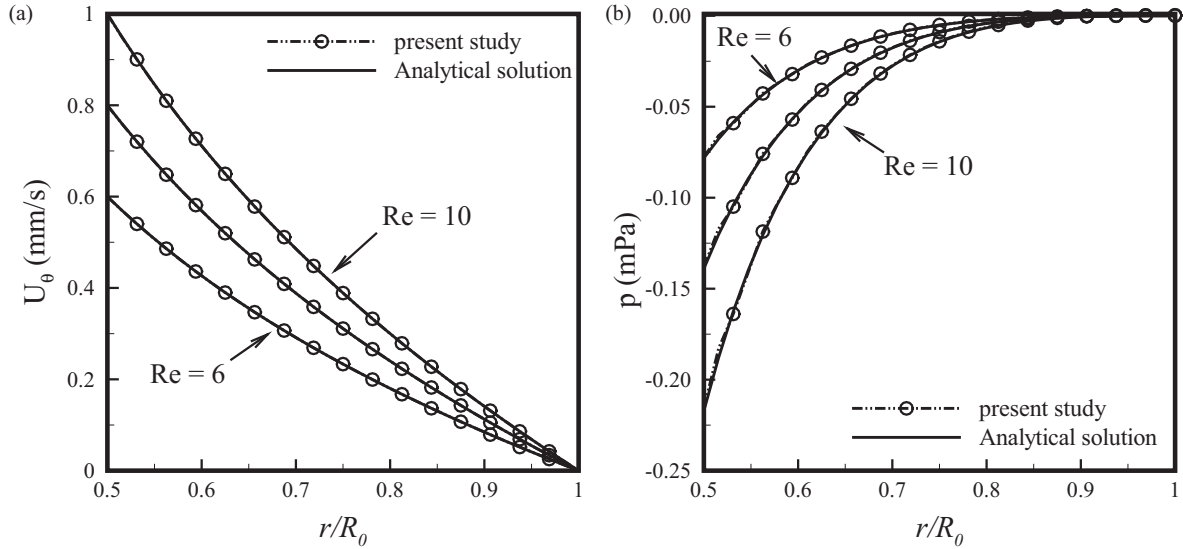


FIG. 11. Comparison between numerical and analytical profiles for different Reynolds numbers: (a) velocity profiles and (b) pressure profiles.

In the above equation,  $r$  is the radial distance. The computational domain is modeled using a square mesh where the radius of inner cylinder consists of  $N_R$  nodes along lattice rows.

For validation purposes, the velocity and pressure profiles are compared with the analytical solutions in Figs. 11(a) and 11(b), respectively, for different Reynolds numbers. The dimensionless relaxation time is set to  $\tau = 0.6$  and a lattice resolution of  $N_R = 32$  is used for simulations.

To measure the accuracy of the present scheme, relative errors of the velocity field  $E_{r(u)}$  for  $Re = 10$  are plotted for several lattice resolutions of  $N_R = 8, 16, 32,$  and  $64$  in Fig. 12, while their corresponding pressure relative errors  $E_{r(p)}$  are presented in Fig. 13. Also included in these figures are numerical results of Verschaeve and Müller [24] and Guo *et al.*

[20]. It must be noted that Eq. (25) is used to calculate relative errors for all fluid nodes and the dimensionless relaxation time is set to  $\tau = 0.6$  for all cases. It can be observed that the present boundary condition provides a more accurate performance in velocity prediction as compared to other schemes.

Clearly, the accuracy of the pressure distribution depends on the accuracy of the density field. As indicated by Bao *et al.* [30], errors in density distribution may be noticeable, when the body force has nonzero value along the wall-normal vector. Therefore, simulation of pressure distribution in this problem is a good challenge for the present boundary treatment since the body force is centripetal here. Considering Fig. 13, it can be observed that Eq. (24) provides acceptable and accurate approximations of density values and,

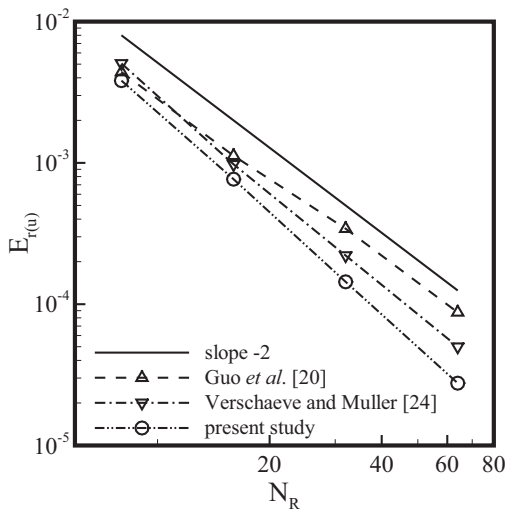


FIG. 12. Comparison of velocity relative errors for different boundary schemes as a function of lattice resolution at  $Re = 10$  for flow between two rotating cylinders.

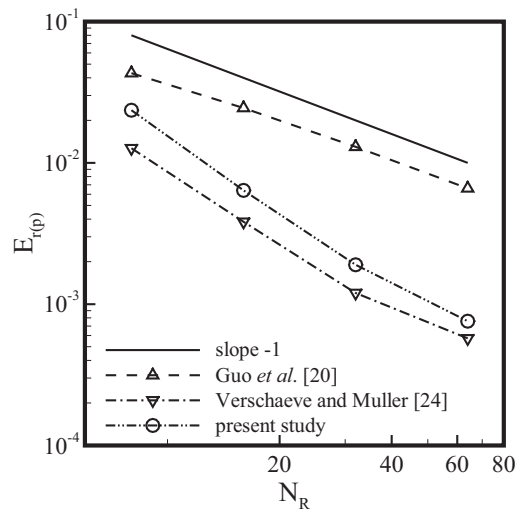


FIG. 13. Comparison of pressure relative errors for different boundary schemes as a function of lattice resolution at  $Re = 10$  for flow between two rotating cylinders.

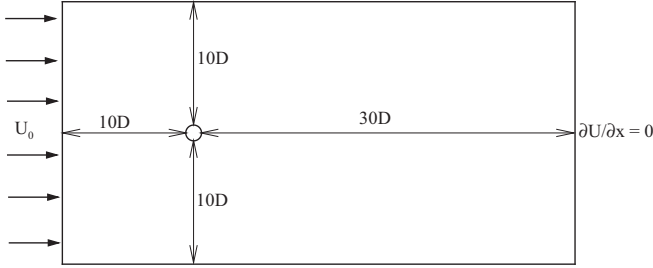


FIG. 14. The geometry of flow around a cylinder.

consequently, pressure distributions. The figure indicates at least first order of accuracy for pressure distribution. The higher order of accuracy for the pressure field in coarse grids as shown in Fig. 13 is in accordance with the findings of Verschaeve and Müller [24] and can be explained with the fact that in coarse grids the density error is higher than first order.

### C. Uniform flow over a cylinder

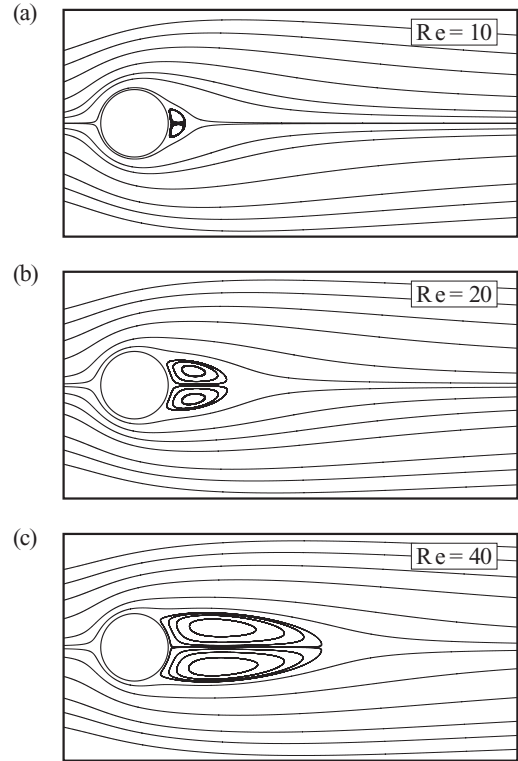
Next validation case for the present boundary treatment is the uniform flow past a circular cylinder, which is a well-documented problem. The flow geometry is shown in Fig. 14, where the outer boundary is located at a distance sufficiently far from the cylinder. The Reynolds numbers of 10, 20, and 40 based on the free stream velocity  $U_0$  and cylinder diameter  $D$  are considered, where the flow remains steady. For all simulations, a domain of  $41D$  by  $21D$  with 30 grid points for each  $D$  is considered. Therefore,  $30 \times 30$  grid points are used to model the cylinder with 112 boundary nodes. The inlet boundary condition is given by a uniform velocity profile, while zero velocity gradients are used at the outlet. Periodic boundary condition is applied to the upper and lower outer boundaries, and the present boundary treatment is used on the circular cylinder.

Figure 15 illustrates the streamlines, where stationary separation bubbles are observed behind the cylinder in all cases. The geometrical configurations of the recirculation regions, such as nondimensional length of recirculation region and separation angle  $\theta_s$ , are compared with published results in Table I. Here, the nondimensional length of recirculation region is defined as  $2L/D$ , where  $L$  is measured from the rearmost point of the cylinder. It is seen that present findings agree reasonably well with those reported in the previous studies [13,31–37].

It is worth mentioning that the calculation of drag force by integrating the total stresses on the surface of the cylinder is relatively simple in the present model. Since the wall-normal vector is used for extrapolation, the total stress including shear stress and pressure can be approximated based on fluid properties of the fluid reference. Considering the transversal velocity of the fluid reference, calculation of shear stress will be straightforward as follows:

$$\tau = \mu \frac{U_{\theta(f)}}{\Gamma}. \quad (29)$$

The pressure is computed on the fluid reference as an approximation of the wall pressure. In contrast to the previous

FIG. 15. Streamlines of steady flow around a cylinder at (a)  $Re = 10$ , (b)  $Re = 20$ , and (c)  $Re = 40$ .

problem, there is no body force here and approximation of density or pressure from the neighborhood is valid. The hydrodynamic force on the cylinder surface can then be obtained by integrating the shear stress and pressure over the entire boundary nodes. The drag coefficient,  $C_D = F_D/(0.5\rho U_0^2)$ , is calculated for three different Reynolds numbers and compared with the results of previous studies in Table II, where reasonable agreements are observed.

In addition to the drag coefficient, the pressure coefficient  $C_p = (p_{\text{wall}} - p_{\infty})/(0.5\rho U_0^2)$  along the cylinder surface is illustrated in Fig. 16 and compared with the numerical results of He and Doolen [38] and Park *et al.* [39] for  $Re = 40$ . It can

TABLE I. Comparison of nondimensional length of recirculation region and separation angles with previous studies.

	Re = 10		Re = 20		Re = 40	
	$2L/D$	$\theta_s$	$2L/D$	$\theta_s$	$2L/D$	$\theta_s$
Fornberg [32]	–	–	1.82	–	4.48	–
Guo and Zhao [34]	0.486	28.13	1.824	43.59	4.168	53.44
Wu and Shu [35]	–	–	1.86	–	4.62	–
Tuann and Olson [36]	0.5	29.7	1.8	44.1	4.2	54.8
Shu <i>et al.</i> [13]	–	–	1.8	–	4.40	–
Nieuwstadt and Keller [37]	0.434	27.96	1.786	43.37	4.357	53.34
Zhou <i>et al.</i> [31]	–	–	1.84	–	4.40	–
Ding <i>et al.</i> [33]	0.504	30	1.86	44.1	4.4	53.5
Present study	0.51	28.1	1.86	42.5	4.58	53.1

TABLE II. Comparison of drag coefficient with previous studies.

	$C_D$		
	Re = 10	Re = 20	Re = 40
Guo and Zhao [34]	3.049	2.048	1.475
Ding <i>et al.</i> [33]	3.07	2.18	1.173
Fornberg [32]	–	2.0001	1.498
Tuann and Olson [36]	3.177	2.253	1.675
Nieuwstadt and Keller [37]	2.828	2.053	1.550
Present study	2.888	2.077	1.561

be seen from Fig. 16 that the present results agree well with those in the literature.

#### D. Solution of Laplace equation in a concentric annulus

In this section, we use the LBGK model presented by Servan Camas and Tsai [40] to solve the Laplace equation in a concentric annulus bounded by two cylinders with different potential values on each cylinder. Laplace equation is one of the simplest elliptic partial differential equations, which is important in many fields of science. This problem is chosen to verify the accuracy and efficiency of the proposed boundary treatment in simulation of curved boundaries for potential fields. In cylindrical coordinates, the Laplace equation is written as follows:

$$\nabla^2 \phi = \frac{1}{r} \frac{\partial}{\partial r} \left( r \frac{\partial \phi}{\partial r} \right) + \frac{1}{r^2} \frac{\partial^2 \phi}{\partial \theta^2} + \frac{\partial^2 \phi}{\partial z^2} = 0. \quad (30)$$

The lattice Boltzmann evolution equation for potential  $\phi$  on 2D discrete lattices can be written as [40]

$$g_i(r + c_i \delta_t, t + \delta_t) - g_i(r, t) = \frac{1}{\tau_\phi} (g_i^{\text{eq}}(r, t) - g_i(r, t)). \quad (31)$$

The corresponding equilibrium distribution of  $g^{\text{eq}}$  on the D2Q9 discrete lattice takes the following form:

$$g_i^{\text{eq}} = \begin{cases} \phi w'_i(1/k) & i > 0 \\ \phi - \sum_{i \neq 0} g_i^{\text{eq}} & i = 0 \end{cases}, \quad (32)$$

where  $w'_{1-4} = 1/3$  and  $w'_{5-8} = 1/12$  are weight factors and  $k$  is a numerical parameter to control the dimensionless relaxation

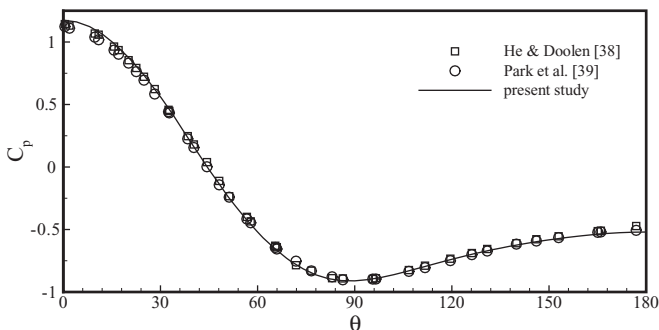


FIG. 16. Comparison of pressure coefficient variations along the cylinder surface for  $Re = 40$ .

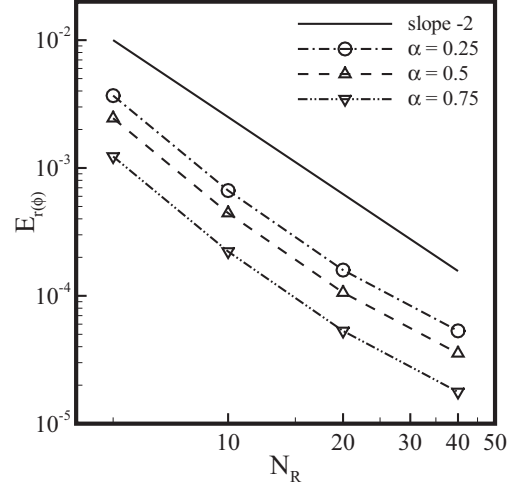


FIG. 17. Relative error of the potential field as function of lattice resolution for different values of potential on the inner and outer cylinders.

time  $\tau_\phi$ , defined as

$$\tau_\phi = k \frac{\delta_t}{\delta_x^2} + \frac{1}{2}. \quad (33)$$

The macroscopic potential is then calculated as  $\phi = \sum_{i=0}^8 g_i$ . In this problem, the potential values on the surface of the inner and outer cylinders are set to be  $\phi_i$  and  $\phi_o$ , respectively. Consequently, the Laplace equation, Eq. (30), has the following analytic solution:

$$\frac{\phi}{\phi_o} = \frac{1 - \alpha}{\log(R_o/R_i)} \log \frac{r}{R_o} + 1, \quad (34)$$

where  $R_i$  and  $R_o$  are inner and outer cylinder radii, respectively, and  $\alpha = \phi_o/\phi_i$ . For modeling,  $N_R = 5, 10, 20, 40$  nodes are considered for inner cylinder radius along lattice rows. Figure 17 shows the dependence of the potential relative error  $E_{r(\phi)}$  on lattice resolution. It is clear that the present boundary treatment satisfies the integrity of the curved boundary to the second order of accuracy.

## VI. CONCLUSION

In the present study, a simple curved-boundary treatment based on a new extrapolation framework is developed, which requires only one equation for extrapolation of macroscopic variables at boundary nodes. Compared with the existing curved-boundary conditions, the proposed treatment is not limited to fluid flow simulations and can simply be extended to potential fields. In particular, an extension of Zou and He [8] boundary scheme is developed by introducing a corrective function for flow simulation, which can be applied to arbitrary 2D boundaries. This corrective function can be easily computed and applied at boundary nodes to enforce the no-slip condition. A series of benchmark test is conducted to validate the accuracy and examine the stability of the proposed boundary condition in simulation of curved boundaries. Numerical results indicate a second order of accuracy for the velocity and potential fields, while

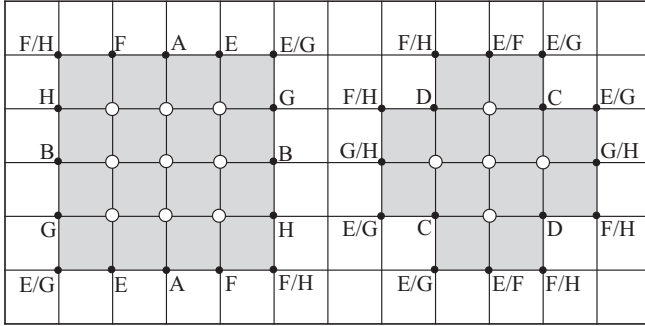


FIG. 18. Boundary configurations for 12 boundary types in a 2D geometry.

at least a first order of accuracy is obtained for the pressure field.

### APPENDIX

In the present boundary treatment, a series of corrective functions is employed to satisfy the no-slip condition in all directions for boundary nodes. According to Eq. (18), there are four unknowns to evaluate corrective functions. In this appendix, a system of equations, which is required to determine these functions, is provided for 12 types of boundaries in a 2D configuration as shown in Fig. 18.

Boundary nodes with three unknown distribution functions are denoted by A, B, C, and D in Fig. 18. For these nodes, the definition of velocity provides two equations and the equality of the nonequilibrium parts in known opposite directions provides the third one. Finally, the system of equations can be closed by setting the remaining unknown corrective function to be zero as follows:

$$\begin{aligned} \text{Node type of A} \rightarrow & \begin{aligned} 2b &= f_1 - f_3 - 2\rho u_x/3 \\ a &= 0 \\ c &= -(a+b)/2 \\ d &= -(a-b)/2 \end{aligned} \end{aligned} \quad (\text{A1})$$

$$\begin{aligned} \text{Node type of B} \rightarrow & \begin{aligned} 2a &= f_2 - f_4 - 2\rho u_y/3 \\ b &= 0 \\ c &= -(a+b)/2 \\ d &= -(a-b)/2 \end{aligned} \end{aligned} \quad (\text{A2})$$

$$\begin{aligned} \text{Node type of C} \rightarrow & \begin{aligned} 2d &= f_6 - f_8 - \rho(u_y - u_x)/6 \\ c &= 0 \\ a &= -c - d \\ b &= -c + d \end{aligned} \end{aligned} \quad (\text{A3})$$

$$\begin{aligned} \text{Node type of D} \rightarrow & \begin{aligned} 2c &= f_5 - f_7 - \rho(u_y + u_x)/6 \\ d &= 0 \\ a &= -c - d \\ b &= -c + d. \end{aligned} \end{aligned} \quad (\text{A4})$$

Boundary nodes with two unknown distribution functions are denoted by E, F, G, and H in Fig. 18. For these nodes, definition of velocity provides two equations and the equality of the nonequilibrium parts in known opposite directions provides the remaining ones as follows:

$$\begin{aligned} \text{Node type of E} \rightarrow & \begin{aligned} 2b &= f_1 - f_3 - 2\rho u_x/3 \\ 2d &= f_6 - f_8 - \rho(u_y - u_x)/6 \\ c &= d - b \\ a &= b - 2d \end{aligned} \end{aligned} \quad (\text{A5})$$

$$\begin{aligned} \text{Node type of F} \rightarrow & \begin{aligned} 2b &= f_1 - f_3 - 2\rho u_x/3 \\ 2c &= f_5 - f_7 - \rho(u_y + u_x)/6 \\ d &= c + b \\ a &= -b - 2c \end{aligned} \end{aligned} \quad (\text{A6})$$

$$\begin{aligned} \text{Node type of G} \rightarrow & \begin{aligned} 2a &= f_2 - f_4 - 2\rho u_y/3 \\ 2d &= f_6 - f_8 - \rho(u_y - u_x)/6 \\ c &= -a - d \\ b &= a + 2d \end{aligned} \end{aligned} \quad (\text{A7})$$

$$\begin{aligned} \text{Node type of H} \rightarrow & \begin{aligned} 2a &= f_2 - f_4 - 2\rho u_y/3 \\ 2c &= f_5 - f_7 - \rho(u_y + u_x)/6 \\ d &= -a - c \\ b &= -a - 2c. \end{aligned} \end{aligned} \quad (\text{A8})$$

For boundary nodes with one unknown distribution function, evaluation of corrective functions is similar to nodes with two unknown distribution functions.

- 
- [1] G. H. Tang *et al.*, *J. Appl. Phys.* **100**, 094908 (2006).  
 [2] M. Wang *et al.*, *J. Colloid Interface Sci.* **304**, 246 (2006).  
 [3] Z. Chai and B. Shi, *Phys. Lett. A* **364**, 183 (2007).  
 [4] M. Wang and S. Chen, *J. Colloid Interface Sci.* **314**, 264 (2007).  
 [5] G. H. Tang, P. X. Ye, and W. Q. Tao, *J. Non-Newton. Fluid Mech.* **165**, 1536 (2010).  
 [6] D. P. Ziegler, *J. Stat. Phys.* **71**, 1171 (1993).  
 [7] X. He *et al.*, *J. Stat. Phys.* **87**, 115 (1997).  
 [8] Q. Zou and X. He, *Phys. Fluids* **9**, 1591 (1997).  
 [9] T. Inamuro, M. Yoshino, and F. Ogino, *Phys. Fluids* **7**, 2928 (1995).  
 [10] S. Chen, D. Martínez, and R. Mei, *Phys. Fluids* **8**, 2527 (1996).  
 [11] Z.-G. Feng and E. E. Michaelides, *J. Comput. Phys.* **195**, 602 (2004).  
 [12] Y. Peng *et al.*, *J. Comput. Phys.* **218**, 460 (2006).  
 [13] C. Shu, N. Liu, and Y. T. Chew, *J. Comput. Phys.* **226**, 1607 (2007).  
 [14] J. Latt, B. Chopard, O. Malaspinas, M. Deville, and A. Michler, *Phys. Rev. E* **77**, 056703 (2008).  
 [15] O. Filippova and D. Hänel, *Int. J. Mod. Phys. C* **09**, 1271 (1998).  
 [16] R. Mei, L.-S. Luo, and W. Shyy, *J. Comput. Phys.* **155**, 307 (1999).  
 [17] R. Mei *et al.*, *J. Comput. Phys.* **161**, 680 (2000).  
 [18] M. h. Bouzidi, M. Firdaouss, and P. Lallemand, *Phys. Fluids* **13**, 3452 (2001).  
 [19] P. Lallemand and L.-S. Luo, *J. Comput. Phys.* **184**, 406 (2003).  
 [20] Z. Guo, C. Zheng, and B. Shi, *Phys. Fluids* **14**, 2007 (2002).  
 [21] X. Kang *et al.*, *Appl. Therm. Eng.* **30**, 1790 (2010).  
 [22] P. H. Kao and R. J. Yang, *J. Comput. Phys.* **227**, 5671 (2008).  
 [23] D. Yu *et al.*, *Prog. Aerosp. Sci.* **39**, 329 (2003).  
 [24] J. C. G. Verschaeve and B. Müller, *J. Comput. Phys.* **229**, 6781 (2010).  
 [25] S. Chen and G. D. Doolen, *Annu. Rev. Fluid Mech.* **30**, 329 (1998).

- [26] X. He and L.-S. Luo, *Phys. Rev. E* **56**, 6811 (1997).
- [27] Z. Guo, B. Shi, and N. Wang, *J. Comput. Phys.* **165**, 288 (2000).
- [28] P. Bhatnagar, E. Gross, and M. Krook, *Phys. Rev.* **94**, 511 (1954).
- [29] I. G. Currie, *Fundamental Mechanics of Fluids* (Marcel Dekker, New York, 2002), pp. xiv.
- [30] J. Bao, P. Yuan, and L. Schaefer, *J. Comput. Phys.* **227**, 8472 (2008).
- [31] H. Zhou *et al.*, *Comput. Meth. Appl. Mech. Eng.* **225-228**, 65 (2012).
- [32] B. Fornberg, *J. Fluid Mech.* **98**, 819 (1980).
- [33] H. Ding *et al.*, *Comput. Meth. Appl. Mech. Eng.* **193**, 727 (2004).
- [34] Z. Guo and T. S. Zhao, *Phys. Rev. E* **67**, 066709 (2003).
- [35] J. Wu and C. Shu, *J. Comput. Phys.* **228**, 1963 (2009).
- [36] S.-y. Tuann and M. D. Olson, *Comput. Fluids* **6**, 219 (1978).
- [37] F. Nieuwstadt and H. B. Keller, *Comput. Fluids* **1**, 59 (1973).
- [38] X. He and G. Doolen, *J. Comput. Phys.* **134**, 306 (1997).
- [39] J. Park, K. Kwon, and H. Choi, *KSME Int. J.* **12**, 1200 (1998).
- [40] B. Servan-Camas and F. T. C. Tsai, *Adv. Water Resour.* **31**, 1113 (2008).